ADVANCED MATERIALS
www.advmat.de

Engraving Copper Foil to Give Large-Scale Binder-Free Porous CuO Arrays for a High-Performance Sodium-Ion Battery Anode

*Shuang Yuan, Xiao-lei Huang, De-long Ma, Heng-guo Wang, Fan-zhi Meng, and Xin-bo Zhang**

As a result of pressing concerns about the imminent exhaustion of fossil fuel resources and the increasing environmental problems, renewable energy sources, such as the wind and the sun, have received intensive attention. Rechargeable batteries, owing to their flexibility, high energy conversion efficiency and simple maintenance, could play an important role in realizing the smooth integration of these intermittent energies into the grid. Although lithium-ion batteries (LIBs) are currently widely used in portable electronic devices and are regarded as the best choice for (hybrid) electric vehicles, we must always be prepared for the exhaustion of the limited and unevenly distributed Li resources in the Earth's crust.[1] In response, room-temperature sodium-ion batteries (NIBs) have again aroused a great deal of interest recently because Na resources are practically inexhaustible and ubiquitous, which is extremely favorable for large-scale stationary electric energy storage applications for renewable energy and smart grids, in which cost and cycle life are more essential factors than energy density.[2,3] However, partly because the Na ion is larger and heavier than the Li ion, some promising anode materials for LIBs are still facing the problems of low capacity, inferior rate capability, poor cycling stability, or even complete electrochemical inactivity in NIBs.[4,5] Therefore, development of advanced anode materials for NIBs is urgently desirable but remains a great challenge.

On the other hand, in a traditional electrode, polymer binder plays an essential role in integrating individual electroactive particles. However, recently the widely used organic binder poly(vinylidene fluoride) (PVDF) has been found to accelerate the deterioration of cycling stability and irreversible capacity losses.[6] Moreover, adding insulating and electrochemically inactive polymer binders would inevitably impede efforts to improve the capacity and rate capability and, furthermore, increase the manufacturing costs of batteries, which is of critical importance for large-scale electric energy storage applications.[6] A binder-free electrode ought to be an effective method to solve this problem. However, a binder-free electrode might be incapable of restraining the morphological collapse during electrochemical reaction. Naturally, porous or array-structured electrodes could provide ample space to accommodate the strain of volume change during charging/discharging processes, facilitate the diffusion of electrolyte into the inner area of the electrodes, and consequently improve the battery performance.[7] Although binder-free and array-structured electrodes have been fabricated on current collectors through various techniques, such as chemical vapor deposition,[8a,b] electrodeposition,[8c] and hydrothermal synthesis,[7b] all these methods suffer from one or more drawbacks, such as the need for special equipment, a complicated preparation process, energy- and time-consuming methods, and difficulties of large scale fabrication at low cost. Therefore, development of a facile and effective strategy for the large-scale and inexpensive fabrication of a high-performance, binder-free electrode with a porous array structure is urgently desirable and of great importance.

Cupric oxide (CuO) is proposed as a promising anode material for LIBs owing to its high theoretical capacity, low cost, abundant sources, and high safety, which is crucial for large-scale electrochemical energy storage. Unfortunately, its practical application in LIBs is still hindered by its low conductivity and morphological collapse caused by the large volume expansion during Li^+ intercalation and deintercalation,[9] which becomes even more serious for NIBs as a result of the larger size of Na^+, and thus have almost kept it off the radar screen in the search for improved electrode materials for LIBs, to say nothing of NIBs. Therefore, it is a coveted goal, but still a big challenge, to enhance significantly the electrochemical performance of CuO in NIBs.

In this Communication, we propose and realize a strategy for scalable fabrication of flexible and porous CuO nanorod arrays (CNAs) by simply engraving commercial copper foils in situ; the foils can then be used directly as the anode for a NIB without addition of any electrochemically inactive conductive agent or polymer binders and further coating processes. The efficacy of this concept is demonstrated by the superior electrochemical performance of the binder-free porous CNA electrode, including a high capacity of over 640 mA h g^{-1} even at a high current density of 200 mA g^{-1}, a high rate (ca. 8C) capability even at room temperature, and good cycling stability.

S. Yuan, Dr. X.-L. Huang, D.-L. Ma, Dr. H.-G. Wang, Dr. F.-Z. Meng, Prof. X.-B. Zhang
State Key Laboratory of Rare Earth Resource Utilization
Changchun Institute of Applied Chemistry
Chinese Academy of Sciences
Changchun, 130022, P. R. China
E-mail: xbzhang@ciac.ac.cn

S. Yuan, D.-L. Ma
Key Laboratory of Automobile Materials
Ministry of Education,
and College of Materials Science and Engineering, Jilin University
Changchun, 130012, P. R. China

DOI: 10.1002/adma.201304469

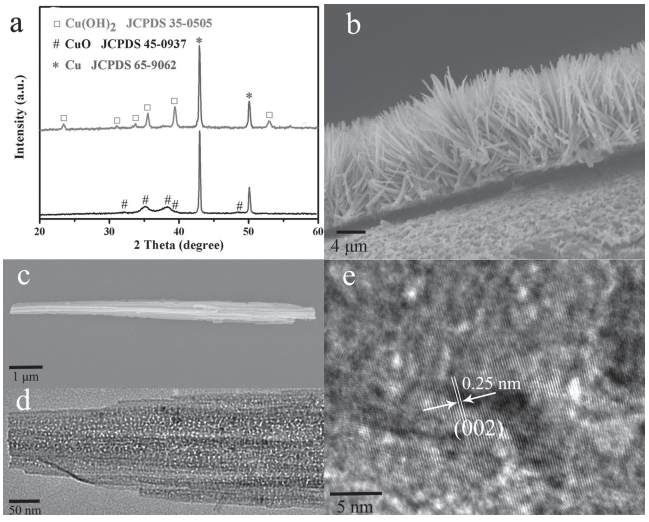

Figure 1. a) XRD patterns of $Cu(OH)_2$ and CuO in situ grown on copper foil. b) SEM image of a CuO nanorod array. c,d) SEM (c) and low magnification TEM (d) images of a single CuO nanorod. e) High resolution image of CuO.

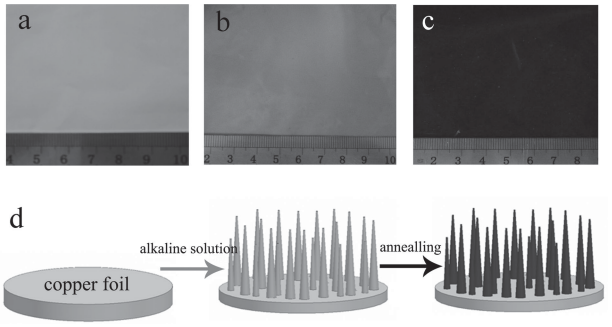

Figure 2. a–c) Optical images of pristine copper foil, a $Cu(OH)_2$ array on Cu foil, and CNAs on Cu foil. d) Scheme of the mechanism for in situ synthesis of CNAs on Cu foil.

The crystal structure of $Cu(OH)_2$ and CuO arrays were first characterized by X-ray diffraction (XRD). As shown in **Figure 1**a, the two strong diffraction peaks at 43.3° and 50.4° come from the Cu substrate (JCPDS file No. 65-9062). All the other diffraction peaks in the red curve can be indexed to orthorhombic $Cu(OH)_2$ (JCPDS file No. 35-0505). After heat treatment (black curve), the diffraction peaks positioned at 32.5°, 35.5°, 38.7°, 38.9°, and 48.7° can be assigned to the $(\bar{1}10)$, (002), (111), (200), and $(\bar{2}02)$ planes of CuO phase (JCPDS file No. 45-0937), respectively. There is no sharp peak that can be indexed to other impurities, which indicates that high purity CuO has been successfully obtained by the facile in situ engraving method. Field-emission scanning electron microscopy (FE-SEM) and transmission electron microscopy (TEM) images were then employed to further characterize the thus obtained samples. As shown in Figure 1b, the CuO was found to be rod-like in structure with a length up to several micrometers. Furthermore, these CuO nanorods are arranged in a favorable array structure, which would facilitate the transfer of the electrolyte and electrons and thus benefit the electrochemical performance (see later). Top-view SEM images of $Cu(OH)_2$ and CuO are shown in Figure S1a,b (Supporting Information). The detailed structure of the CuO nanorods was then further investigated by TEM. More obviously, the low-magnification SEM and TEM images in Figures 1c and d show that the diameters of the CuO nanorods range from a few tens of nanometers to hundreds of nanometers. Furthermore, it was found that the surface of CuO nanorod is rough and contains holes. This porous structure was further confirmed by the nitrogen (N_2) absorption–desorption isotherms (Figure S2a, Supporting Information), which show type-IV isotherms and indicate a mesoporous morphology of the CuO nanorods. The pore diameter distribution was estimated from the isotherm adsorption branch using the Barrett–Joyner–Halenda (BJH) model; the size of most of the pores was less than 20 nm (Figure S2b). Figure 1e shows a high resolution TEM image of a CuO nanorod. The marked interplanar *d* spacing of 0.25 nm corresponds to the (002) lattice plane of monoclinic CuO.

The growth process of the above confirmed CNAs can be visually tracked by the color changes of the Cu substrate. At the outset, the fresh Cu foil is yellow and the surface is relatively smooth (**Figure 2**a). After being engraved in alkaline solution, the surface changes to light blue and becomes a little rough, consistent with in situ formation of $Cu(OH)_2$ directly on the Cu foil substrate (Figure 2b), which is then converted to black CNAs after heat treatment at 200 °C for 3 h under vacuum (Figure 2c). Combining this with all the above obtained results (Figure 2d), we proposed a possible but different[8d–f] reaction mechanism. The oxidation step provides the Cu^{2+} ions necessary for coordination self-assembly. Under basic alkaline solution conditions with O_2, a $Cu(NH_3)_n^{2+}$ complex is first generated: $Cu^{2+} + 4NH_3 \rightarrow Cu(NH_3)_4^{2+}$;[9a] subsequently OH^- replaces the NH_3 in the $Cu(NH_3)_n^{2+}$ complex, giving rise to a $Cu(OH)_2$ array: $Cu(NH_3)_4^{2+} + 2OH^- \rightarrow Cu(OH)_2 + 4NH_3\uparrow$.[9a] After annealing, CNAs are finally obtained in situ on the copper foil. Furthermore, thanks to the absence of special equipment and a facile and mild process, CNAs of this kind can be prepared on a large scale at low cost. Moreover, as the CNAs are grown in situ by engraving of the Cu foil, the foil can be used directly as a flexible electrode in NIBs (Figure S3a, Supporting Information). The absence of polymer binder avoids the binder swelling problem and thus would theoretically enhance the structural stability and thus the cycle performance.[6] Even more important, the absence of non-conducting polymeric binder could offer high Na^+ flux and continuous and fast conducting pathways for electrons throughout the electrode,[7] which would benefit the electrochemical performance of NIBs.

Coin cells with a metallic Na counter electrode were assembled, and the galvanostatic charge/discharge technique was used to evaluate the electrochemical performance of a binder-free CNA electrode. As shown in **Figure 3**a, in the first discharge process, the CNA electrode demonstrates a high initial discharge capacity of 935 mA h g^{-1} with a slope region from 1.9 to 1.2 V and a clear plateau at ca. 0.45 V. The initial Coulombic efficiency is 61%, wherein possible electrolyte degradation and formation of a solid-electrolyte interphase (SEI) layer at the CuO nanorod surface cannot be excluded.[9b,10] After the first cycle, a stable discharge capacity of ca. 640 mA h g^{-1} can

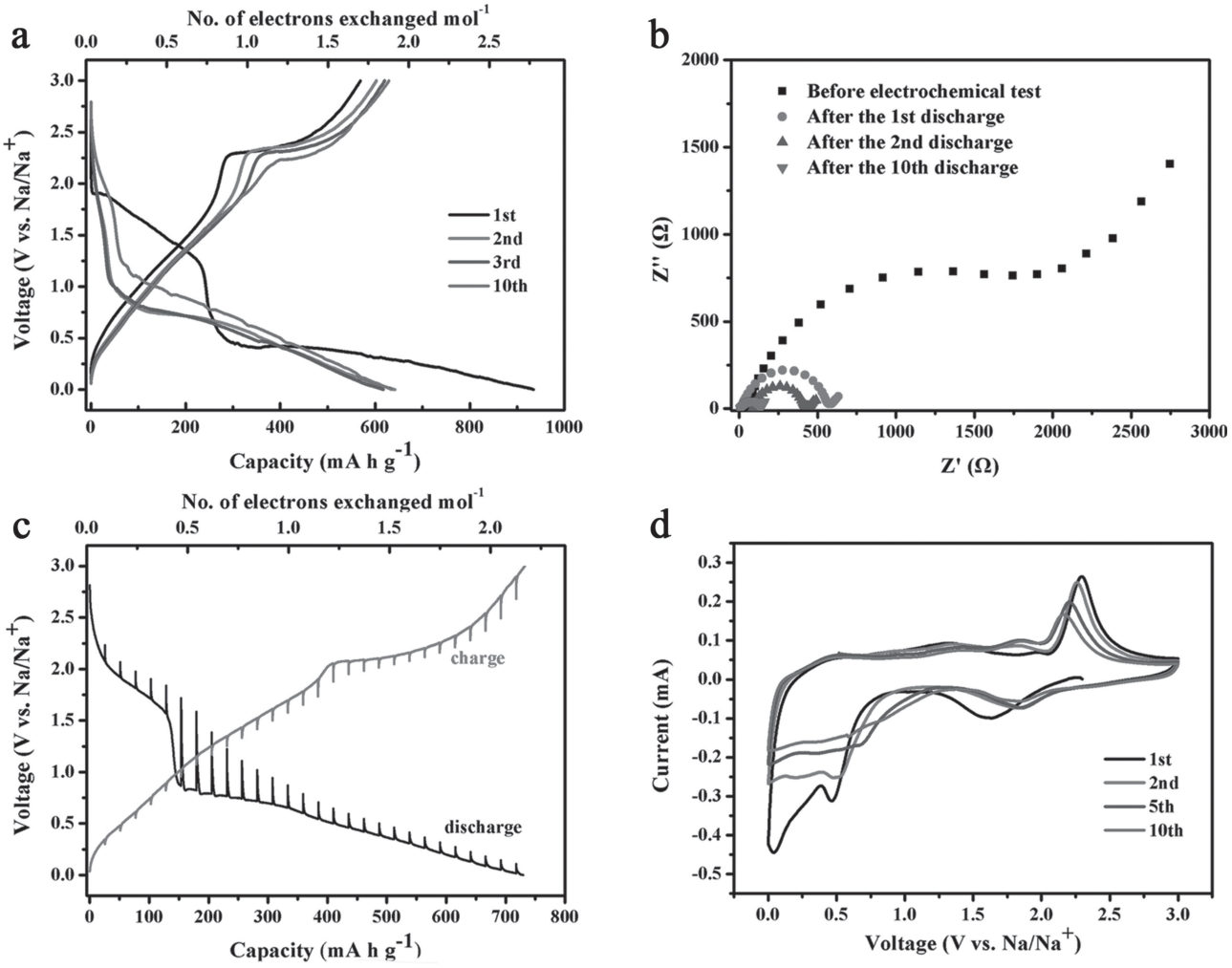

Figure 3. a) Electrochemical performance of binder-free CNA electrode at a current density of 20 mA g^{-1}. b) EIS of CNA electrode. c) GITT profile of CNA electrode at a current density of 20 mA g^{-1}. d) CV curves of the CNA electrode with a scan rate of 0.2 mV s^{-1} between 0 and 3.0 V.

be obtained, which corresponds to 1.9 sodium ions per formula unit and is thus very close to the theoretical capacity of CuO (674 mA h g^{-1}), indicating that the formed SEI film during the first cycle is robust enough. Furthermore, it is found that, with increasing cycle number, the overpotentials of both the charging and discharging processes gradually decrease. This activation process can be attributed to the increasing conductivity of the CNA electrode during Na^+ insertion and the reduction of the size of CuO during cycling,[11a,b] which is confirmed by the electrochemical impedance spectroscopy (EIS) (Figure 3b), wherein a decrease in the total resistance is observed with increasing number of cycles. Furthermore, to get a discharge curve closer to the thermodynamic equilibrium, the battery is charged to 3.0 V vs. Na before the discharge is started by using the galvanostatic intermittent titration technique (GITT) mode. Figure 3c presents the quasi-equilibrium redox potential of the CNA electrode at a current density of 20 mA g^{-1}. It is found that the shape of the GITT curve is very similar to the above obtained discharge–charge curve under continuous charge and discharge, indicating that even in the continuous discharge–charge process, the material is very close to the equilibrium, which might be due to the good ionic and electronic conductivities of the CNAs.[11c] Cyclic voltammetry (CV) was then employed to further understand the electrochemical reactive processes of binder-free CNAs. Figure 3d depicts the CV curves of porous CNAs vs. Na in the range of 0–3 V at a scan rate of 0.2 mV s^{-1}. It is found that, during the first discharging process, there are three reduction peaks, located at 1.6, 0.46, and 0.05 V, corresponding to multi-step electrochemical reactions that involve the generation of intermediate copper oxide phase ($Cu^{II}_{1-x}Cu^{I}_{x}O_{1-x/2}$), the formation of Cu_2O phase, and the decomposition of Cu_2O into Cu and Na_2O, respectively.[9b,10] Subsequently, during the charging process, four oxidation peaks are found at about 0.5, 1.3, 1.85, and 2.3 V. The small peaks positioned at 0.5 and 1.3 V can be assigned to the oxidation of a small amount of residual Cu_2O into CuO, while the 1.85 V peak corresponds to the process $2Cu + Na_2O \rightarrow Cu_2O + 2Na$. The fourth peak, at 2.3 V, might result from the oxidation of just formed Cu_2O into CuO.[9b,10] In the subsequent cycles, the CV curves are very similar in shape except that reduction and oxidation peaks shift to higher

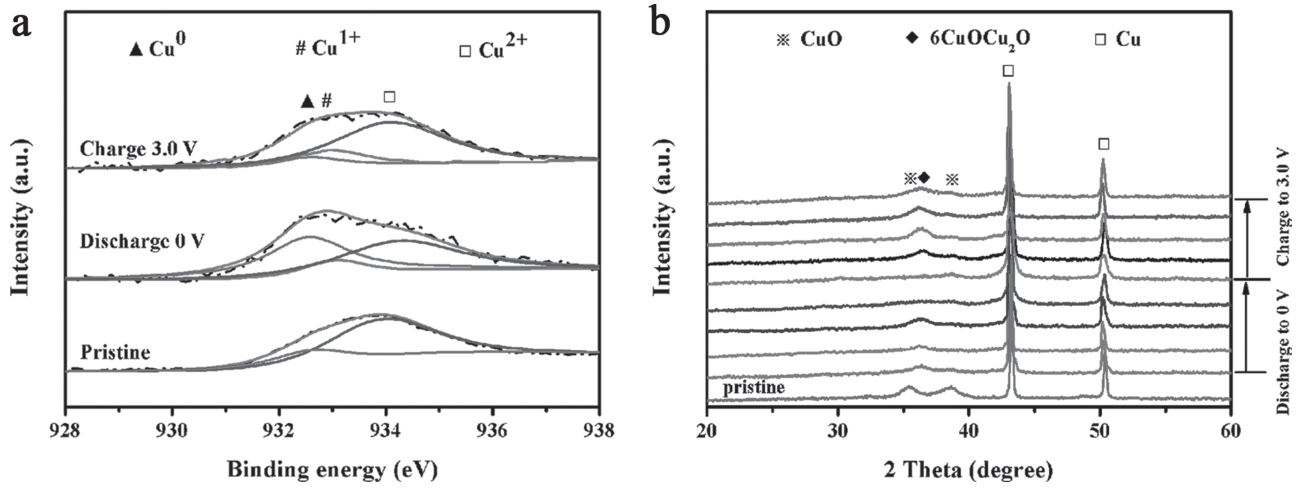

Figure 4. XPS spectra (a) and ex situ XRD patterns (b) of CNAs at different charge and discharge states.

and lower potential, respectively, indicating that the overpotentials are gradually decreased, which is consistent with the above discharge–charge and EIS results and would benefit the energy conversion efficiency and power density.

To further identify the phase evolution of CuO during the electrochemical reaction, X-ray photoelectron spectroscopy (XPS) and XRD were employed at different charge and discharge states of the CNA electrode. As shown in **Figure 4**, before the electrochemical test, the peak can be assigned to Cu^{2+} (934.1 eV) while no detectable Cu^{1+} (932.9 eV) peak can be found, indicating the high purity of the in situ formed CuO, which is consistent with the above mentioned XRD result. The weak Cu^0 peak might arise from the Cu substrate. After discharging to 0 V, the intensity of the Cu^{2+} peak decreases, while the peak intensity of Cu^0 (932.6 eV) becomes stronger and the Cu^{1+} peak emerges, corresponding to the reduction reaction from CuO to Cu_2O and Cu^0.[10] These processes can be reversed during the following charging process. After charging to 3.0 V, the Cu^{2+} peak recovers, owing to the oxidation reaction from Cu to Cu_2O and further formation of CuO.[10] It should be noted that the Cu^0 peak can also be observed, indicating that there are some residual Cu particles in the recharged CNA electrode. Naturally, these in situ generated Cu particles could construct a metallic Cu conducting matrix and ensure the desired homogeneous and intimate contact with active component, which might also be responsible for the above observed improved electrochemical performance (Figure 3a) and increase of conductivity (Figure 3b) upon cycling. Similarly, the ex situ XRD patterns (Figure 4b) show that the intensities of CuO peaks (35.5° and 38.7°) decrease progressively during the reduction reaction of CuO, and the new peak positioned at 36.3° can be assigned to the generated intermediate composite copper oxide phase ($6CuOCu_2O$, JCPDS file No. 03-0879). After charging to 3.0 V, the phase of $6CuOCu_2O$ remains, which is consistent with the above XPS results (Figure 4a). It should be noted that no sharp peaks of Na_2O and Cu_2O and CuO phases can be found after the discharge and charge process, indicating that their crystallinities are poor, which would benefit the kinetics of subsequent Na^+ insertion/extraction reaction.[11d] This merit, when coupled with the in situ generated, highly conductive Cu network, could attribute to enhanced electrochemical performance on cycling.

Figure 5a shows the cycling performance of CNAs investigated by the galvanostatic charge and discharge method between 0 and 3.0 V at a current density of 50 mA g^{-1}. For comparison, CNAs scraped off of copper foil and CuO nanosheet electrodes with a different binder were also investigated (the morphologies of scraped CuO and CuO nanosheet are shown in Figure S4 in the Supporting Information). Surprisingly, when PVDF is used as the binder, very low specific capacities of 8.1 and 112 mA h g^{-1} can be obtained for CuO nanosheet and the scraped CuO nanorods, respectively, which might be due to their very low conductivity, although higher capacities of 99.9 and 140 mA h g^{-1}, respectively, can be obtained by adding acetylene black (ACET) to improve the conductivity, which is still much lower than that of the in situ generated porous, binder-free CNA electrode. Even after 30 discharge–charge cycles, a high capacity of 542 mA h g^{-1} capacity can still be obtained, which is more than 542% and 387% times higher than that of the CuO nanosheets and scraped CNAs electrode, respectively. These significantly improved specific capacities and cycling stability of the CNA electrode can be attributed to the unique array structure and to the fact that the electrode does not include a binder.

Another outstanding feature of the binder-free CNA electrode is the rate capability. As shown in Figure 5b, the binder-free CNA electrode shows much higher capacity than the scraped CNAs and CuO nanosheet electrodes, even with the addition of highly conductive ACET, under all investigated current densities (0.02–1 A g^{-1}). Unexpectedly, even at the very high current density of 1 A g^{-1} (ca. 8C rate, a rate of nC corresponds to full discharge in $1/n$ hours), the CNAs electrode can still deliver a high specific capacity of nearly 200 mA h g^{-1} after 60 cycles, which is much higher than for electrodes with PVDF binder and conductive ACET (only ca. 40 mA h g^{-1}). Furthermore, even under a high current density of 200 mA g^{-1}, a high coulombic efficiency (near 100%) and specific capacity (290.6 mA h g^{-1})

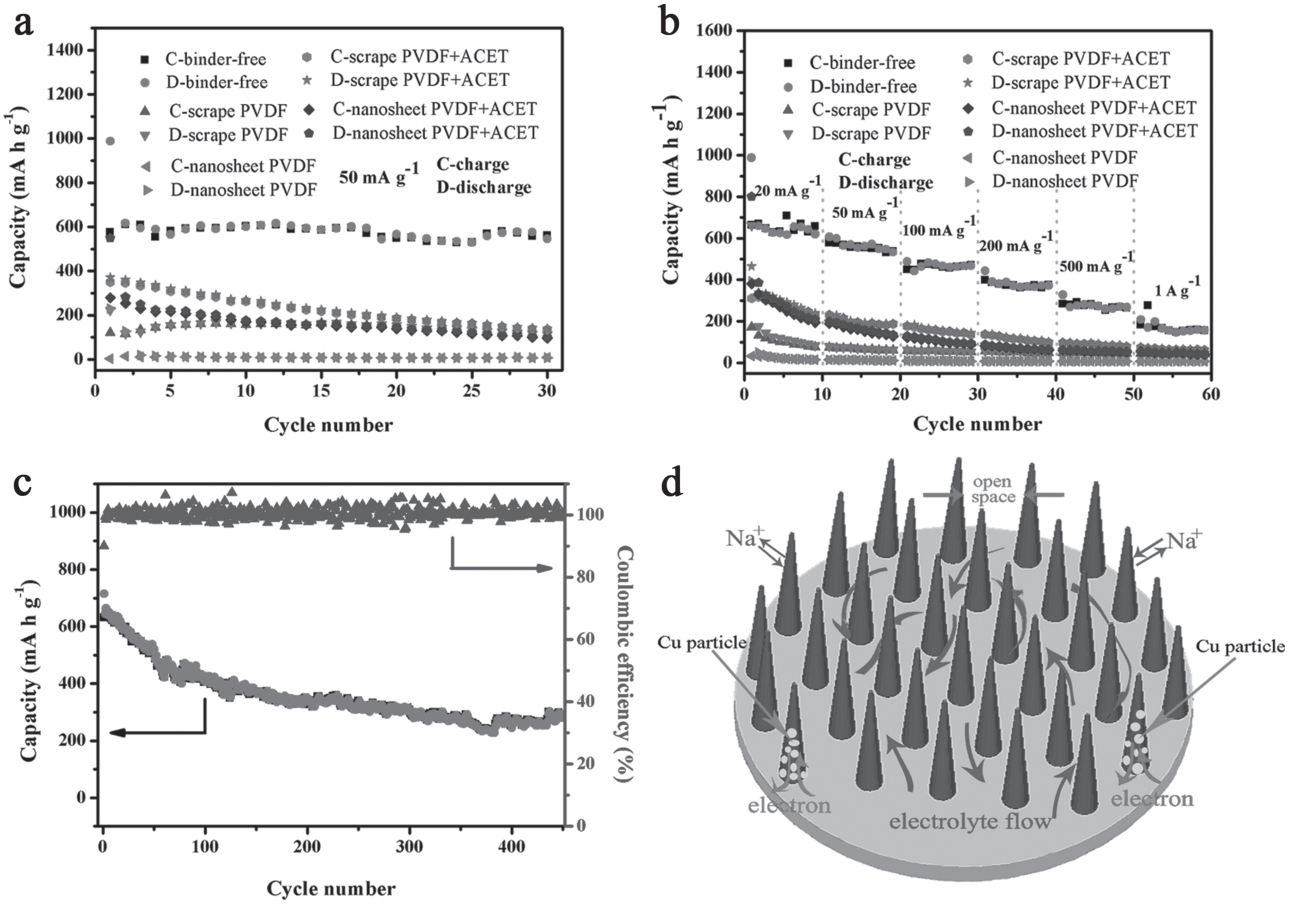

Figure 5. a) Cycling performance of binder-free porous CNAs, CuO nanorods scraped off of Cu foil, and CuO nanosheets. b) Rate capability of different CuO electrodes at various current densities from 0.02 to 1 A g^{-1}. c) Cycling performance of binder-free CNA electrode at a high current density of 200 mA g^{-1}. d) Schematic diagram showing the strategy for binder-free CNA electrode.

can be achieved even after 450 cycles (Figure 5c), corresponding to a capacity retention of 45.2% and a small capacity loss of 0.78 mA h g^{-1} per cycle.

The above obtained superior electrochemical performance of the CNA electrode might reasonably be attributed to the unique array structure and the binder-free architecture (Figure 5d). As shown in Figure S5 (Supporting Information), aligned CNAs can still be found in SEM images of the CNA binder-free electrode after 450 discharge–charge cycles. The CNAs electrode also keeps its original flexibility and no CuO is detached from the copper substrate even after 450 cycles (Figure S3b).[13a-c] It should be noted that Na^+ cannot be inserted into the oxide-ion array of CuO, and thus the retention of morphological integrity on passing from the crystalline to an amorphous phase that conducts electrons as well as Na^+ ions might be attributed to its porous nanorod structure, wherein the pores of each CuO nanorod and ample open space between neighboring nanorods not only allowed for easy diffusion of electrolyte into the inner area of the electrodes but also allowed the electrochemical activity of CuO to be efficiently utilized and accommodation of the volume variation during the Na uptake and release process, which could restrain the pulverization and exfoliation of CuO nanorods from the current collector,[7c,d,12] Second, the in situ fabricated free-standing and aligned porous CNAs ensure good electronic contact between CuO nanorods and the Cu current collector, which theoretically facilitates electrons flowing between the substrate and CNAs.[7c,d,12] Furthermore, the electrochemical reaction starts from the bottom of the CuO array (as electrons can only come from the contacted Cu substrate) and then gradually spreads to the whole electrode, which not only helps to retain morphological integrity of the CNAs, but also allows the in situ formed interconnected metallic Cu particles to serve as electron transporting paths between the Cu substrate and the unreacted CuO close to the tips of the CNAs.[7c,12] Third, the absence of electrochemically inactive and insulated of polymeric binder could facilitate high Na^+ flux, with continuous and fast conducting pathways throughout the electrode.[13d,14] On other hand, it should be noted that the poor energy-storage efficiency and large irreversible capacity loss on initial charging might hinder the practical application. To this end, conductive coating and/or doping of the CNAs and presodiation methods should be employed to decrease the overpotentials (improve the energy-storage efficiency) and restrain the large irreversible capacity loss on the initial charge, respectively.

In summary, we have proposed and realized a facile and scalable in situ engraving Cu foil method for preparing aligned porous CNAs that offer many advantages, including porous structure, ample open space, and short and fast electron transporting paths. Furthermore, the thus obtained CNAs are free-standing and intrinsically integrated with the Cu substrate and thus could be directly used as an anode for NIBs without adding other inactive materials such as carbon black or polymer binder during additional electrode fabrication processes. As a result of the desirable electrode architecture, the binder-free CNAs electrodes exhibit superior electrochemical performance, including high capacity of over 640 mA h g^{-1} even at a high current density of 200 mA g^{-1}, high rate capability even at room temperature, and good cycle stability up to 450 cycles. The obtained promising electrochemical results and scientific understanding could provide a design principle and encourage more research into other high-performance and low cost anodes for next-generation high energy density NIBs.

Experimental Section

Synthesis of CNAs: All the chemicals were of analytical grade and used as purchased without further purification. Copper foil was supplied by Shenzhen Weifeng Power Technology Ltd Co. (P. R. China). Hydrochloric acid, sodium hydroxide, and ammonium hydroxide were supplied by Beijing Chemical Works. In a typical procedure for synthesizing CNAs, Cu foil was washed with hydrochloric acid and subsequently washed with deionized water several times to remove surface impurities. The washed Cu foil was then immediately immersed into 200 mL of water containing 0.5 mL of ammonia (28%) and 40 mg of sodium hydroxide at room temperature. Then the Cu foil with a layer of blue copper hydroxide was taken out of the solution, washed with deionized water several times, and then dried in air. To obtain CNAs, the Cu foils were heated at 200 °C for 3 h under vacuum.

Material Characterization: Powder XRD measurements were performed on a Bruker D8 Focus powder X-ray diffractometer using Cu K_α (λ = 0.15406 nm) radiation (40 kV, 40 mA). SEM was performed on a field emission Hitachi S-4800 instrument operated at an accelerating voltage of 10 kV. TEM was performed with a FEI Tecnai G_2 S-Twin instrument having a field-emission gun operated at 200 kV. Nitrogen adsorption measurements were performed on a Micromeritics ASAP 2020 adsorption analyzer. Pore sizes were estimated from pore size distribution curves from the adsorption isotherms using the BJH method. XPS spectra were obtained with an ESCALAB MK II X-ray photoelectron spectrometer with an Al K_α source.

Electrochemical Measurement: CNAs were directly used as an electrode without added conductive agent and polymeric binder. The average mass loading of CuO on Cu foil was ca. 2.0 mg cm^{-2}. The 2025 coin-type cells were assembled in an argon-filled glove box, and pure Na foils were used as the counter electrode. The electrolyte was 1 M $NaPF_6$ in a mixture of ethylene carbonate, dimethyl carbonate, and 5% fluoroethylene carbonate. Galvanostatic charge–discharge cycling tests were performed with a Land CT2001A battery testing system (Land, P. R. China) at room temperature. Impedance and the cyclic voltammetry measurements were performed with a VMP3 electrochemical workstation (Bio-Logic, France).

Supporting Information

Supporting Information is available from the Wiley Online Library or from the author.

Acknowledgements

This work was financially supported by the 100 Talents Program of The Chinese Academy of Sciences, the National Program on Key Basic Research Project of China (973 Program, Grant No. 2012CB215500), the Foundation for Innovative Research Groups of the National Natural Science Foundation of China (Grant No. 20921002), and the National Natural Science Foundation of China (Grant No. 21101147).

Received: September 5, 2013
Revised: November 5, 2013
Published online: January 20, 2014

[1] a) M. Armand, J. M. Tarascon, *Nature* **2008**, *451*, 652; b) N. Yabuuchi, M. Kajiyama, J. Iwatate, H. Nishikawa, S. Hitomi, R. Okuyama, R. Usui, Y. Yamada, S. Komaba, *Nat. Mater.* **2012**, *11*, 3309; c) L. M. Sou, Y. S. Hu, H. Li, M. Armand, L. Q. Chen, *Nat. Commun.* **2013**, *4*, 1481; d) Y. Sun, L. Zhao, H. Pan, X. Lu, L. Gu, Y. S. Hu, H. Li, M. Armand, Y. Ikuhara, L. Q. Chen, X. J. Huang, *Nat. Commun.* **2013**, *4*, 1870.

[2] a) K. Saravanan, C. W. Mason, A. Rudola, K. H. Wong, P. Balaya, *Adv. Energy Mater.* **2012**, *3*, 444; b) K. H. Ha, S. H. Woo, D. Mok, N. S. Choi, Y. Park, S. M. Oh, Y. Kim, J. Kim, J. Lee, L. F. Nazar, K. T. Lee, *Adv. Energy Mater.* **2013**, *3*, 770; c) H. G. Wang, Z. Wu, F. L. Meng, D. L. Ma, X. L. Huang, L. M. Wang, X. B. Zhang, *ChemSusChem* **2013**, *6*, 56; d) H. L. Pan, Y. S. Hu, L. Q. Chen, *Energy Environ. Sci.* **2013**, *6*, 2338; e) Y. Wang, X. Yu, S. Xu, J. Bai, R. Xiao, Y. S. Hu, H. Li, X. Q. Yang, L. Q. Chen, X. J. Huang, *Nat. Commun.* **2013**, *4*, 2365.

[3] a) H. Zhu, Z. Jia, Y. Chen, N. Weadock, J. Wan, O. Vaaland, X. Han, T. Li, L. B. Hu, *Nano Lett.* **2013**, *13*, 3093; b) L. Zhao, J. Zhao, Y. S. Hu, H. Li, Z. Zhou, M. Armand, L. Q. Chen, *Adv. Energy Mater.* **2012**, *2*, 962; c) Y. Kim, Y. Park, A. Choi, N. S. Choi, J. Kim, J. Lee, J. H. Ryu, S. M. Oh, K. T. Lee, *Adv. Mater.* **2013**, *25*, 3045; d) P. Senguttuvan, G. Rousse, M. E. Arroyo y de Dompablo, H. Vezin, J. M. Tarascon, M. R. Palacin, *J. Am. Chem. Soc.* **2013**, *135*, 3897–3903; e) X. Yu, H. Pan, W. Wan, C. Ma, J. Bai, Q. Meng, S. N. Ehrlich, Y. S. Hu, X. Q. Yang, *Nano Lett.* **2013**, *13*, 4721.

[4] a) J. Qian, X. Wu, Y. Cao, X. Ai, H. X. Yang, *Angew. Chem. Int. Ed.* **2013**, *52*, 4633; b) J. Song, M. Xu, L. Wang, J. B. Goodenough, *Chem. Commun.* **2013**, *49*, 5280; c) D. Su, H. J. Ahn, G. X. Wang, *Chem. Commun.* **2013**, *49*, 3131; d) L. Wu, X. H. Hu, J. Qian, F. Pei, F. Wu, R. Mao, X. Ai, H. X. Yang, Y. L. Cao, *J. Mater. Chem. A* **2013**, *1*, 7181.

[5] a) V. Palomares, P. Serras, I. Villaluenga, K. B. Hueso, J. C. Gonzalez, T. Rojo, *Energy Environ. Sci.* **2012**, *5*, 5884; b) A. Darwiche, C. Marino, M. T. Sougrati, B. Fraisse, L. Stievano, L. Monconduit, *J. Am. Chem. Soc.* **2012**, *134*, 20805; c) A. Abouimrane, D. Dambournet, K. W. Chapman, P. J. Chupas, W. Weng, K. Amine, *J. Am. Chem. Soc.* **2012**, *134*, 4505; d) J. Fullenwarth, A. Darwiche, A. Soares, B. Donnadieu, L. Monconduit, *J. Mater. Chem. A* **2014**, DOI: 10.1039/C3TA13976J.

[6] a) B. Koo, H. Kim, Y. Cho, K. T. Lee, N. S. Choi, J. Cho, *Angew. Chem. Int. Ed.* **2012**, *51*, 8762; b) M. H. Ryou, J. Kim, I. Lee, S. Kim, Y. K. Jeong, S. Hong, J. H. Ryu, T. S. Kim, J. K. Park, H. Lee, J. W. Choi, *Adv. Mater.* **2013**, *25*, 1571; c) I. Kovalenko, B. Zdyrko, A. Magasinski, B. Hertzberg, Z. Milicev, R. Burtovyy, I. Luzinov, G. Yushin, *Science* **2011**, *334*, 75; d) F. F. Xia, X. L. Hu, Y. M. Sun, W. Luo, Y. H. Huang, *Nanoscale* **2012**, *4*, 4707.

[7] a) J. Jiang, Y. Li, J. P. Liu, X. Huang, C. Yuan, X. W. Lou, *Adv. Mater.* **2012**, *24*, 5166; b) C. Zhou, Y. W. Zhang, Y. Y. Li, J. P. Liu, *Nano Lett.* **2013**, *13*, 2078; c) L. Yu, L. Zhang, H. B. Wu, G. Q. Zhang, X. W. Lou, *Energy Environ. Sci.* **2013**, *6*, 2664; d) N. Du, H. Zhang,

B.-D. Chen, J.-B. Wu, X.-Y. Ma, Z.-H. Liu, Y.-Q. Zhang, D. R. Yang, X.-H. Huang, J.-P. Tu, *Adv. Mater.* **2007**, *19*, 45058.

[8] a) C. K. Chan, H. Peng, G. Liu, K. McIlwrath, X. F. Zhang, R. A. Huggins, Y. Cui, *Nat. Nanotechnol.* **2008**, *3*, 31; b) H. Zhang, X. Yu, P. V. Braun, *Nat. Nanotechnol.* **2011**, *6*, 277; c) Y. Liu, Y. Xu, Y. Zhu, J. N. Culver, C. A. Lundgren, K. Xu, C. S. Wang, *ACS Nano* **2013**, *7*, 3627; d) W. Zhang, X. Wen, S. Yang, Y. Berta, Z. L. Wang, *Adv. Mater.* **2003**, *15*, 822; e) J. P. Liu, X. T. Huang, Y. Li, K. M. Sulieman, X. He, F. L. Sun, *J. Mater. Chem.* **2006**, *16*, 4427; f) W. X. Zhang, Z. H. Yang, S. X. Ding, S. H. Yang, *Solid State Phenom.* **2007**, *121–123*, 303.

[9] a) R. Rodríguez-Clemente, C. J. Serna, M. Ocaña, E. Matijević, *J. Cryst. Growth* **1994**, *143*, 277; b) J. Y. Xiang, J. P. Tu, L. Zhang, Y. Zhou, X. L. Wang, S. J. Shi, *J. Power Sources* **2010**, *195*, 313; c) Y. Jiang, Z. Yang, W. Luo, X. L. Hu, Y. H. Huang, *Phys. Chem. Chem. Phys.* **2013**, *15*, 2954.

[10] a) C. K. Wu, M. Yin, S. O'Brien, J. T. Koberstein, *Chem. Mater.* **2006**, *18*, 6054; b) J. C. Park, J. Kim, H. Kwon, H. Song, *Adv. Mater.* **200 9**, *21*, 803; c) F. Han, D. Li, W. C. Li, C. Lei, Q. Sun, A. H. Lu, *Adv. Funct. Mater.* **2012**, *23*, 1692.

[11] a) B. Liu, P. Soares, C. Checkles, Y. Zhao, G. H. Yu, *Nano Lett.* **2013**, *13*, 3414; b) P. Poizot, S. Laruelle, S. Grugeon, L. Dupont, J. M. Tarascon, *Nature* **2000**, *407*, 496; c) R. Berthelot, D. Carlier, C. Delmas, *Nat. Mater.* **2011**, *10*, 74; d) Y. L. Liu, Y. Xu, X. Han, C. Pellegrinelli, Y. Zhu, H. Zhu, J. Wan, A. C. Chung, O. Vaaland, C. S. Wang, L. B. Hu, *Nano Lett.* **2012**, *12*, 5664.

[12] a) Y. G. Li, B. Tan, Y. Wu, *Nano Lett.* **2008**, *8*, 265; b) K. Wang, H. P. Wu, Y. Meng, Z. X. Wei, *Small* **2013**, DOI: 10.1002/smll.201301991; c) J. Yan, A. Sumboja, E. Khoo, P. S. Lee, *Adv. Mater.* **2011**, *23*, 746; d) Z. P. Song, T. Xu, M. L. Gordin, Y. B. Jiang, I. T. Bae, Q. F. Xiao, H. Zhan, J. Liu, D. H. Wang, *Nano Lett.* **2012**, *12*, 2205.

[13] a) K. T. Lee, J. Cho, *Nano Today* **2011**, *6*, 28; b) C. Jiang, E. Hosono, H. S. Zhou, *Nano Today* **2006**, *1*, 28; c) P. G. Bruce, B. Scrosati, J. M. Tarascon, *Angew. Chem. Int. Ed.* **2008**, *47*, 2930; d) X. L. Huang, R. Z. Wang, D. Xu, Z. L. Wang, H. G. Wang, J. J. Xu, Z. Wu, Q. C. Liu, Y. Zhang, X. B. Zhang, *Adv. Funct. Mater.* **2013**, *23*, 4345.

[14] a) M. M. Rahman, J. Z. Wang, M. F. Hassan, S. L. Chou, Z. X. Chen, H. K. Liu, *Energy Environ. Sci.* **2011**, *4*, 952; b) H. Xiong, M. D. Slater, M. Balasubramanian, C. S. Johnson, T. Rajh, *J. Phys. Chem. Lett.* **2011**, *2*, 2560.